Faraday Discussions

Cite this: *Faraday Discuss.*, 2022, **238**, 161

PAPER

Crossed-beam and theoretical studies of multichannel nonadiabatic reactions: branching fractions and role of intersystem crossing for O(^{3}P) + 1,3-butadiene†

C. Cavallotti, *[a] A. Della Libera,[a] C.-W. Zhou, [bc] P. Recio, [d] A. Caracciolo, [d] N. Balucani *[d] and P. Casavecchia *[d]

Received 8th February 2022, Accepted 29th March 2022
DOI: 10.1039/d2fd00037g

Atomic oxygen reactions can contribute significantly to the oxidation of unsaturated aliphatic and aromatic hydrocarbons. The reaction mechanism is started by electrophilic O atom addition to the unsaturated bond(s) to form "chemically activated" triplet oxy-intermediate(s), which can evolve adiabatically on the triplet potential energy surface (PES) and nonadiabatically *via* intersystem crossing on the singlet PES, forming intermediates that undergo unimolecular decomposition to a variety of bimolecular product channels. Here, we apply a combined crossed molecular beam (CMB)–theoretical approach to the study of the O(^{3}P) + 1,3-butadiene reaction. Although the kinetics of this reaction have been extensively investigated, little is known about the primary products and their branching fractions (BFs). In the present work, a total of eight product channels were observed and characterized in a CMB experiment at a collision energy of 32.6 kJ mol^{-1}. Synergic *ab initio* transition-state theory-based master equation simulations coupled with nonadiabatic transition-state theory on coupled triplet/singlet PESs were employed to compute the product BFs and assist the interpretation of the CMB experimental results. The good agreement found between the theoretical predictions and CMB experiments supported the use of the adopted methodology for the prediction of channel-specific rate constants as a function of temperature and pressure suitable to be used for the kinetic modeling of 1,3-butadiene oxidation and of systems where 1,3-butadiene is an important intermediate.

[a]*Dipartimento di Chimica, Materiali e Ingegneria Chimica "Giulio Natta", Politecnico di Milano, 20131 Milano, Italy. E-mail: carlo.cavallotti@polimi.it*

[b]*School of Energy and Power Engineering, Beihang University, Beijing, 100191, PR China*

[c]*Combustion Chemistry Centre, School of Chemistry, Ryan Institute, National University of Ireland, Galway, H91 TK33, Ireland*

[d]*Dipartimento di Chimica, Biologia e Biotecnologie, Università degli Studi di Perugia, 06123 Perugia, Italy. E-mail: piergiorgio.casavecchia@unipg.it; nadia.balucani@unipg.it*

† Electronic supplementary information (ESI) available: Crossed-beam experimental results for O(^{3}P) + 1,3-butadiene, thermal rate constants (0.1, 1, 10 atm and 300–2200 K), master equation inputs. See DOI: 10.1039/d2fd00037g

1. Introduction

The reactions between ground state atomic oxygen, $O(^3P)$, and unsaturated hydrocarbons (UHs) have an impact on a large variety of gaseous chemical and physical systems, going from combustion flames[1–8] to plasma discharges,[9] and to the Earth's atmosphere.[10] In addition, they also play an important role in the reactivity of oxygen-rich interstellar and circumstellar environments,[11–13] as well as in the upper atmosphere of Titan.[14,15]

During the oxidation of UHs and AHs (aromatic hydrocarbons) by $O(^3P)$, the "chemically activated" triplet oxy-intermediate(s) formed following electrophilic O atom addition to the unsaturated bond(s), can evolve adiabatically on the triplet potential energy surface (PES) and/or nonadiabatically (*via* intersystem crossing, ISC) on the singlet PES, undergoing unimolecular decomposition to a variety of bimolecular product channels. In recent years, this picture has been documented in several multichannel nonadiabatic reactions of $O(^3P)$ with 2C, 3C, and 4C UHs, such as ethylene,[16–19] propene,[20] propyne,[21,22] allene,[23,24] 1-butene,[25] 1,2-butadiene,[26] and AHs, such as benzene,[27,28] by combining, in a synergistic fashion, crossed-molecular-beam (CMB) experiments with theoretical calculations of the underlying triplet/singlet PESs and statistical calculations of product branching fractions (BFs), taking into account ISC. The theoretical and experimental predictions[20,28] were found to be in good agreement also with several kinetic studies on various $O(^3P)$ reactions with UHs using product detection by ionization with tunable vacuum ultraviolet synchrotron radiation.[29,30] The capability of the developed model to reconcile CMB and kinetic thermal experiments, which differ significantly for operative conditions, supported the theoretical foundations of the model and allowed us to obtain a qualitative interpretation of the reactive dynamics of these systems that we used to develop rate rules for the whole $O(^3P)$ + alkene reaction class.[31] According to this model, the reactivity is started on the triplet PES by oxygen addition to form an adduct, which can then decompose (but not isomerize) or perform ISC to the singlet PES, and then dissociate, isomerize, or undergo collisional stabilization. Recently, Ramasesha *et al.*[32] found that this reaction mechanism is not adequate to predict the reactivity of cyclopentene with $O(^3P)$, as they found evidence that ISC does not take place from the entrance well, but from an isomer formed after ring opening and H-transfer on the triplet PES. The authors suggested that this peculiar reactivity could be due to the cyclic nature of the reactant. We believe that this is a reasonable explanation, as ring opening should have a rate constant similar to that of other bond breaking reactions that take place on the triplet PES for other $O(^3P)$ + alkene systems we have studied, such as for example in propene + $O(^3P)$, the pathway leading to the formation of H_2CO + CH_3CH.[33] Following ring opening, it is then possible that other isomerization reactions on the triplet PES become competitive with ISC.

In the present work, we apply the synergistic experiment–theory approach we developed for this class of reactions to the study of the $O(^3P)$ + 1,3-butadiene reaction, a system of interest for atmospheric and combustion kinetics both from a fundamental and an applied perspective. From a fundamental standpoint, 1,3-butadiene is the simplest alkene with two conjugated double bonds. It can thus serve as a prototype to study the kinetics of $O(^3P)$ + alkene with

conjugated dienes. In this respect, it will be interesting to check whether the simple reaction scheme we proposed for the $O(^3P)$ + alkene reaction class can be extended to this system. From an application perspective, an accurate knowledge of 1,3-butadiene reaction chemistry is necessary to further develop models of PAHs and soot formation. It is in fact known that 1,3-butadiene is a significant intermediate towards the formation of large hydrocarbons during the combustion of olefins in flames.[5,34–38] Furthermore, it is also among the possible precursors to benzene formation through several addition reactions of C2 to C4 hydrocarbons.[39–42] 1,3-butadiene is also an air pollutant due to its toxic nature.[43,44] Although the primary use of 1,3-butadiene is the production of synthetic rubber, it is nevertheless found in ambient air in urban and suburban areas as a consequence of its emission from motor vehicles, both from its presence in fuels and as a combustion product.[6,8,45]

Because of its relevance, the $O(^3P)$ + 1,3-butadiene global reaction kinetics have been extensively studied at room and higher temperatures ($k_{\{298K\}} \approx 2 \times 10^{-11}$ cm^3 per molecule per s).[46–51] However, little is known about the nature of its primary products and BFs. In 2000, Laskin *et al.*[52] did a kinetic modeling experiment on the oxidation of 1,3-butadiene and suggested that the main channels of this reaction are the elimination of atomic and molecular hydrogen, as well as the formation of CO and H_2CO (formaldehyde). However, combustion models of 1,3-butadiene flames were still not satisfactory because of the lack of detailed knowledge about the nature of the possible primary products and their BFs as a function of temperature. In 2018, Zhou *et al.*[7] performed a detailed chemical kinetic mechanism (AramcoMech 3.0) and experimental study of 1,3-butadiene combustion over a wide range of temperature, pressure, and equivalence ratios. They found that $O(^3P)$ addition to 1,3-butadiene greatly influences the fuel reactivity from intermediate to high temperatures (>800 K). However, in the mechanism, the $O(^3P)$ + 1,3-butadiene reaction kinetics were derived by analogy with those of $O(^3P)$ + propene.[20] Thus, three possible product channels were considered: H + C_3H_5O, H_2CO + C_3H_4, and C_2H_3 (vinyl) + CH_2CHO (vinoxy), with H elimination being the minor channel and the vinoxy radical formation the main one. A sensitivity analysis showed that this reaction, and in particular the reaction channel leading to H_2CO + C_3H_4, is the most important in inhibiting ignition delay times at temperatures higher than 950 K. The reason is that this pathway acts as a chain termination reaction, while the other two are branching steps, as they lead to the formation of two radicals. The proper determination of the partition of the reactive flux between termination and branching pathways therefore plays a central role in determining the reaction kinetics of this system.[7,52] In this framework, the aim of this paper is to investigate the $O(^3P)$ + 1,3-butadiene reaction with the intent of understanding its chemical dynamics and determining BFs and rate constants that can be used for future kinetic simulations of systems in which this reaction plays an important role.

The paper is organized as follows. In section 2, we describe the experimental and theoretical methods adopted to investigate the title reaction. In section 3, we first report the PES that we used to interpret the reactivity of this system, followed by the experimental results, and the results of the ME simulations in CMB conditions and as a function of temperature. A general discussion of the results is given in the Master equation section, before the conclusions.

2. Methods

2.1 Experimental technique

The experiments were carried out using a CMB apparatus featuring two supersonic beam sources of the reactants crossing at 90°, a rotatable quadrupole mass spectrometer detector with both hard (70 eV) and soft (17 eV) electron ionization, and a real-time TOF (time-of-flight) system for reactants and products. The apparatus has been described in some detail elsewhere.[21,53–57] For the present study, the atomic oxygen beam was generated using a supersonic beam source[53,58,59] in which a 5% O_2/He gas mixture, at a pressure of 8.5 kPa (85 mbar), was discharged through a 0.48 mm diameter water-cooled quartz nozzle at 300 W of RF power, followed by a 1.0 mm diameter boron nitride skimmer and a further collimating aperture. The atomic oxygen beam mainly contains $O(^3P)$ and a small amount of $O(^1D)$ ($\leq$10%).[59] Under the present experimental conditions, the reactive scattering is expected to be dominated by $O(^3P)$ (see the ESI†). The molecular beam of 1,3-butadiene was obtained by expanding 57.3 kPa (573 mbar) of the neat gas (99.3% gas purity) through a 0.1 mm diameter stainless-steel nozzle, followed by a 0.8 mm skimmer, and a further defining aperture. In these conditions, the reactant velocities were 2180 and 715 m s^{-1}, with speed ratios of 4.7 and 5.9 for the oxygen and 1,3-butadiene beams, respectively. The resulting collision energy was 32.6 kJ mol^{-1}. Product laboratory angular distributions at selected mass-to-charge (m/z) ratios were acquired by modulating the 1,3-butadiene beam at 160 Hz for background subtraction. Product TOF distributions were measured by the pseudo-random chopping method at 6 μs per channel.

Quantitative information on the reaction dynamics was derived from the raw data by moving from the laboratory (LAB) to the center-of-mass (CM) coordinate systems and by analyzing the product angular, $T(\theta)$, and translational energy, $P(E_T')$, distributions into which the CM product flux can be factorized.[55,57] The best-fit CM functions were derived from the forward convolution fit of the total product LAB angular, $N(\theta)$, and TOF distributions, $N(\theta, t)$, at a specific mass-to-charge (m/z) ratio value, according to the relation: $I_{CM}(\theta, E_T')_{total} = \sum_i w_i[T(\theta)P(E_T')]_i$. As described elsewhere,[57] the best-fit values of w_i allow the derivation of the relative yields of the different channels. It should be noted that with this technique, in which the number density of the scattered products is detected, heavy and thus slow products in the CM system, which are left by a light co-product (such as a H atom), are strongly amplified in the LAB system because of the favorable Jacobian transformation which relates the LAB number density $N(\theta,v)$ to the CM flux $I(\theta,u)$ through the relation $N(\theta,v) = I_{CM}(\theta,u)v/u^2$, where v and u and the LAB and CM product velocity, respectively. During the data analysis, the quantity $I_{CM}(\theta,u)_{total}$ is usually expressed in terms of the product translational energy, $P(E_T')$, as $I_{CM}(\theta, E_T')$.

2.2 Theoretical methods

The system reactivity was investigated using the *ab initio* transition state theory-based master equation methodology[60] we have used in recent years to study several reactions of addition of $O(^3P)$ to unsaturated hydrocarbons[20–22,25,26,33] and

benzene.[27,28] This computational procedure is composed of three steps: investigation of the PES through electronic structure calculations, determination of the rate constants of elementary steps using the form of transition state theory (TST) that is most suitable for the specific reaction channel (variational or conventional), and determination of rate constants, solving the master equation. Details are reported below for each step.

The C_4H_6O PES was investigated by determining the structures of the stationary points (wells and saddle points) at two levels of theory. At the lowest level of theory (Level 0), a preliminary scan of all relevant wells and reaction channels was performed using the ωB97X-D functional[61] and the 6-311+G(d,p) basis set. Structures were then refined at the ωB97X-D/aug-cc-pVTZ level (Level 1), which is also used to compute Hessians. When necessary, such as, for example, for $O(^3P)$ addition to the terminal carbon atom of 1,3 butadiene, structures and energies along the minimum energy paths (MEPs) were determined at Level 1 of theory. This was, however, not the case for barrierless reactions, for which MEP structures were determined at the CASPT2 level. Energies were computed at two levels of theory. For stationary points with single reference character (generally with T1 diagnostic values smaller than 0.03), high level energies (HL) were determined on Level 1 structures at the CCSD(T) level corrected with a density fitted (DF) MP2 extrapolation to the complete basis set (CBS) and with corrections for core electron excitations as:

$$E(\mathrm{HL}) = E(\mathrm{CCSD}(T)/\text{aug-cc-pVTZ}) + [E(\mathrm{CCSD}(T,\mathrm{core})/\text{cc-pVTZ}) - E(\mathrm{CCSD}(T)/\text{cc-pVTZ})] + [E(\text{DF-MP2/CBS}) - E(\text{DF-MP2/aug-cc-pVTZ})] \quad (1)$$

where E(MP2/CBS) is defined as:

$$E(\text{DF-MP2/CBS}) = E(\text{DF-MP2/aug-cc-pVTZ})] + 0.58[E(\text{DF-MP2/aug-cc-pVQZ}) - E(\text{DF-MP2/aug-cc-pVTZ})]. \quad (2)$$

The E(MP2/CBS) extrapolation was performed using Martin's two parameter scheme.[62] For systems with high multireference character, energies were computed at the CASPT2/aug-cc-pVTZ level on Level 1 structures using active spaces (AS) selected to include all orbitals and electrons directly involved in the reactive process. More specific details on the adopted active spaces are reported in the Results section. The minimum energy crossing point (MECP) between triplet and singlet PESs was determined at Level 1 of theory using the methodology recently implemented in EStokTP.[28,63] All Level 0 and Level 1 electronic structure calculations were performed with Gaussian 09,[64] while DF-MP2, CCSD(T), and CASPT2 calculations were performed with Molpro.[65]

Rate constants for reactions passing from a distinct transition state (TS) were evaluated using conventional TST, with partition functions determined in the rigid rotor harmonic oscillator (RRHO) approximation. Internal torsional motions were described using the 1D hindered rotor (HR) approximation, computing the associated partition functions from the 1D-HR eigenvalues. Vibrational frequencies were then computed after projecting the torsional motion from the Hessian. Rate constants for seven barrierless reactions on the singlet PES were determined using variable reaction coordinate TST (VRC-TST).[66] A dedicated publication on the reactivity of the singlet PES and the implementation

of VRC-TST in EStokTP is in preparation, which will report specific details on the study of these barrierless reactions. Here, we only mention that the VRC-TST stochastic scan of the 6 dimensional space defined by the transitional coordinates was performed at the CASPT2(2e,2o)/cc-pVDZ level using correction potentials for geometry relaxation and energy determined along the MEP on structures optimized at the CASPT2 level with large ASs (inclusive of all π bonding and antibonding orbitals and of the σ and σ^* orbitals of the breaking bond) and with energies determined with the same AS and the aug-cc-pVTZ basis set. A standard 0.9 correction factor for recrossing was used to scale the VRC-TST rate constants. The rate constant for ISC from the triplet to the singlet PES was determined from the MECP using non adiabatic TST (NA-TST)[67] as implemented in EStokTP[63] using Level 1 singlet and triplet Hessians. ISC probabilities were computed using Landau–Zener theory.[68] Spin–orbit couplings (SOC) between singlet and triplet PESs were determined using a Breit-Pauli Hamiltonian with Molpro.[65] The three components of the coupling matrix computed with symmetry adapted wave functions were then square root averaged to compute a single SOC, which was then adopted for the determination of the ISC probabilities.

Master equation (ME) simulations were performed using our stochastic MC-RRKM code,[69,70] which implements NA-TST and is therefore able to account explicitly for the coupling between the singlet and triplet PESs. Two distinct ME simulations were performed, depending on whether the triplet PES is accessed from addition to the terminal or central C atoms. The branching fraction for addition at the terminal and central carbon atoms for CMB simulations was determined at 300 K, thus implicitly assuming that the energy of the beam does not contribute to the density of states (DOS) at the TS. A total of 10^4 stochastic simulations was performed for each examined condition. Thermal simulations were performed in the 300–2200 K and 0.1–10 bar temperature and pressure ranges, respectively, in an Ar thermal bath. The intermolecular collisional energy transfer was calculated with Lennard-Jones collisional rates using $\sigma = 4.21$ Å and $\varepsilon = 331$ K average Lennard-Jones parameters and a single exponential down model with an average downward energy computed as $\Delta E_{down} = 395(T/300)^{0.49}$ cm^{-1}, determined following the procedures suggested by Jasper.[71]

3. Results and discussion

3.1 Potential energy surface

The triplet and singlet potential energy surfaces determined theoretically and then used to investigate the reactivity that follows the addition of O(^{3}P) to 1,3-butadiene are shown in Fig. 1a and b, respectively.

The initial step of the O(^{3}P) + 1,3-C_4H_6 reaction is O(^{3}P) addition on the triplet PES to the terminal or central carbon atom. Depending on the entrance well, the reactive system evolves along two different pathways. Oxygen addition to the 1,3-C_4H_6 terminal carbon atom leads to the formation of ^{3}W1. The energy barrier, -2.1 kJ mol^{-1}, is slightly submerged with respect to the reactants. It should be noted that, differently from what was found for the reactions between O(^{3}P) and alkenes, there is no barrier if calculations are performed at the ωB97X-D/aug-cc-pVTZ level, both if energies are computed at the ωB97X-D and CCSD(T) levels. However, this is not the case when energies are computed on ωB97X-D structures at the CASPT2 level using a (8e,7o) active space formed by the oxygen (4e,3o) p

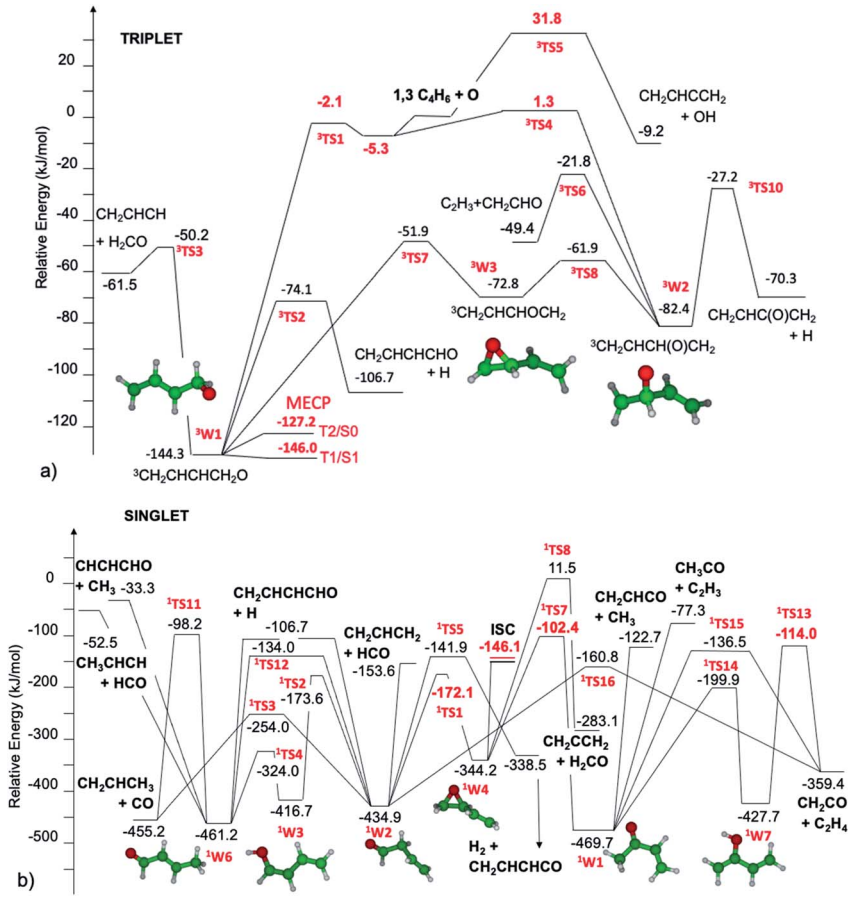

Fig. 1 Schematic representation of the O(^{3}P) + 1,3-butadiene triplet (a) and singlet (b) potential energy surfaces. Relative energies (kJ mol^{-1}, 0 K) computed at the CCSD(T)/CBS and CASPT2/aug-cc-pVTZ levels (in red) on ωB97X-D/aug-cc-pVTZ level structures.

electrons and orbitals and the (4e,4o) π and π* bonding and antibonding orbitals of 1,3-butadiene in Fig. 1. The significant impact of the theoretical level used for the calculations on the estimated energy barriers (or lack thereof) for the entrance channels is a consequence of the multireference nature of O(^{3}P) addition to alkenes, as described by Sabbah *et al.* in a seminal paper.[72] The CASPT2 barrier height is about 3 kJ mol^{-1} from the entrance van der Waals well, which is common to both addition channels and lies about 5.3 kJ mol^{-1} below the reactants. Four reaction channels are possible for ^{3}W1: decomposition to H_2CO and the $^3CH_2CHCH$ diradical, H β-scission to form the $CH_2CHCHCHO$ radical, isomerization to the ^{3}W3 oxirane well, and ISC to the singlet PES. There are interesting similarities and differences with respect to the reaction mechanisms of O(^{3}P) with alkenes. The bond breaking reactions leading to H_2CO and H formation are quite similar to those we observed for propene.[20] The energy barrier for H_2CO formation from ^{3}W1 (94 kJ mol^{-1}) is slightly higher than that found for propene (81 kJ mol^{-1}), while those for H β-scission are similar (69.9 *vs.*

61.9 kJ mol^{-1}). The most notable difference is the isomerization reaction pathway by which ^{3}W1 can be converted to the oxirane diradical well ^{3}W3, which can then further isomerize to ^{3}W2. The existence of a relatively fast isomerization pathway between the two entrance wells ^{3}W1 and ^{3}W2 is related to the presence of the conjugated π bonds, which allow the formation of the relatively stable intermediate well ^{3}W3. As will be discussed in section 3.3, this pathway is of particular relevance for what concerns O(^{3}P) addition to the central carbon atom. Similarly to what was found for alkenes, the structure of the MECP between the triplet and singlet PESs is near that of the entrance well. Differently from what was found for alkenes, the T2/S0 and T1/S1 energies differ substantially by about 20 kJ mol^{-1}, while the SOCs are similar: 31.2 and 36.8 cm^{-1}, respectively. This means that ISC will take place much faster from the T1 electronic state than from the T2 state. Following ISC, it is reasonable to expect rapid S1/S0 internal conversion.

Oxygen addition to the 1,3-C_4H_6 central carbon atom leads to the formation of ^{3}W2. The small energy barrier for addition, 1.3 kJ mol^{-1} with respect to the reactants, means that addition to the terminal carbon is favored at low temperatures. It is interesting to notice that the HL energy barrier, 9.5 kJ mol^{-1}, is much higher than the CASPT2 energy. This means that BFs for addition at the terminal and central carbon atoms differ substantially if computed using a single or multiple reference approach. The entrance well, ^{3}W2, can evolve along three different reaction paths: H β-scission, decomposition to C_2H_3 + CH_2CHO, and isomerization to ^{3}W1 through ^{3}W3. ISC to the singlet PES may also be possible, but according to our previous studies of alkene[20] reactivity, this pathway is not competitive with the fast decomposition channels that can be accessed following addition to the central carbon atom. In particular, for this system, isomerization to ^{3}W3 requires overcoming a small energy barrier, 20.5 kJ mol^{-1}, thus indicating that this is a fast reaction pathway.

The singlet PES is accessed through ISC from ^{3}W1. As shown in the PES diagram presented in Fig. 1b, we assume that the whole reaction flux going through ISC proceeds to the formation of the oxirane well ^{1}W4. This is a simplification of what is likely to be the reactivity of this system following ISC. Detailed studies of ISC for O(^{3}P) + C_2H_4 (ref. 17, 18 and 73) and O(^{3}P) + C_3H_6 (ref. 20 and 30) have in fact shown that the diradical singlet formed upon ISC can follow three reaction pathways: isomerization to the oxirane well (^{1}W4), to the aldehyde well (^{1}W2) through H transfer, or formation of an unsaturated ketene upon H_2 loss. The determination of the proper partition of the fluxes requires some complicated analysis of the reactivity of the intermediate species formed following ISC, which has strong multireference character and is, for the reasons explained above, in the S1 excited state. However, some specificities of this system indicate that it is reasonable to describe its reactivity assuming that the whole reaction flux goes to the ^{1}W4 well. In fact, differently from what was found for propene[20] and 1-butene,[25] the two main pathways for the isomerization of ^{1}W4, leading to ^{1}W2 and ^{1}W1, have very different energy barriers. The reason is that isomerization to 3-butenal (^{1}W2) is favored over isomerization to methyl vinyl ketone (^{1}W1) by the resonant stabilization of the TS. The two isomerization TSs for ^{1}W4, ^{1}TS1 and ^{1}TS7, have strong diradical multireference character, with one radical centered on the oxygen atom and one on the carbon atom whose bond with oxygen is broken in the reactive process. It is this second radical, which is centered on the central carbon atom, that in ^{1}TS1 can take advantage of resonance stabilization with the

π bond of the spectator vinyl group, while this is not possible for ^{1}TS7, where the radical is located on the terminal carbon atom. As a consequence, the energy barriers for ^{1}TS1 and ^{1}TS7 from ^{1}W4, computed at the CASPT2/aug-cc-pVTZ level to properly describe their multireference character, are 172 and 242 kJ mol^{-1}, respectively, thus indicating that the most favored reaction channel for ^{1}W4 leads to the formation of 3-butenal (^{1}W2). This reaction mechanism is well described by assuming that the whole ISC reactive flux leads to ^{1}W4, as this well will eventually evolve to ^{1}W2 and there is thus no need to account for the possible direct formation of ^{1}W2 after ISC. The 3-butenal well ^{1}W2 has two barrierless decomposition pathways to CH_2CHCH_2 + HCO and $CH_2CHCHCHO$ + H, which can eliminate CO to give C_3H_6, or isomerize to the 2-butenal ^{1}W6 well through two pathways: directly through ^{1}TS12 or *via* keto–enol tautomerization *via* ^{1}TS2 and ^{1}TS4. The 2-butenal well ^{1}W6 has three barrierless decomposition pathways to CH_3CHCH + HCO, $CH_2CHCHCHO$ + H, and CH_3 + CHCHCHO, and one elimination reaction leading to CO and C_3H_6. An alternative pathway suggested in the literature[74] to lead to CO + C_3H_6, in which 2-butenal isomerizes to a ketene intermediate that then eliminates CO, has been investigated as well and was found to not be competitive with the pathways reported in Fig. 1b. The vinyl methyl ketone well ^{1}W1, which is the minimum energy well among those considered in the present investigation, can be accessed from ^{1}W4 and then further reacts though two barrierless decomposition channels, leading to C_2H_3 + $COCH_3$ and C_2H_3CO + CH_3, or decomposes to C_2H_4 + CH_2CO through two pathways.

Additional details on the reactivity on the singlet PES, concerning in particular the AS used for CASPT2 calculations and details of VRC-TST calculations will be published in a companion paper on the study of the reactivity of 2-butenal, 3-butenal, and methyl vinyl ketone.

3.2 Experimental results

The energetically allowed primary product channels of the title reaction that have been experimentally observed in this work are listed below. The reaction enthalpies are those derived from the present electronic structure calculations (accuracy ±4 kJ mol^{-1}) (see Fig. 1).

$$O(^3P) + 1,3\text{-}C_4H_6 \rightarrow CH_2CHCHCHO + H,\ \Delta H_0^0 = -106.7\ \text{kJ mol}^{-1} \quad (3)$$

$$\rightarrow CH_2CHCOCH_2 + H,\ \Delta H_0^0 = -70.3\ \text{kJ mol}^{-1} \quad (4)$$

$$\rightarrow CH_2CHCHCO + H_2,\ \Delta H_0^0 = -338.5\ \text{kJ mol}^{-1} \quad (5)$$

$$\rightarrow C_3H_6 + CO,\ \Delta H_0^0 = -455.2\ \text{kJ mol}^{-1} \quad (6)$$

$$\rightarrow CH_2CO + C_2H_4,\ \Delta H_0^0 = -359.4\ \text{kJ mol}^{-1} \quad (7)$$

$$\rightarrow C_3H_5\ (\text{allyl}) + HCO,\ \Delta H_0^0 = -153.6\ \text{kJ mol}^{-1} \quad (8)$$

$$\rightarrow CH_2CHO + C_2H_3,\ \Delta H_0^0 = -49.4\ \text{kJ mol}^{-1} \quad (9)$$

$$\rightarrow CH_3CO + C_2H_3,\ \Delta H_0^0 = -77.4\ \text{kJ mol}^{-1} \quad (10)$$

$$\rightarrow H_2CO + C_3H_4 \text{ (allene)}, \Delta H_0^0 = -283.3 \text{ kJ mol}^{-1} \quad (11)$$

$$\rightarrow H_2CO + CH_2CHCH, \Delta H_0^0 = -61.5 \text{ kJ mol}^{-1} \quad (12)$$

The CH_3 elimination channels, leading to CH_3 + CH_2CHCO and CH_3 + CHCHCHO, are also exothermic ($\Delta H_0^0 = -122.6$ and -33.5 kJ mol^{-1}, respectively) (see Fig. 1); however, CH_3 was found below detectable limits which, within our sensitivity, puts it at a BF $\leq$ 1–2%. The direct H abstraction forming OH is slightly exothermic ($\Delta H_0^0 = -9.2$ kJ mol^{-1}), but has a barrier of 31.8 kJ mol^{-1} (Fig. 1a), which makes it negligible under our experimental conditions (see, for instance, Fig. 4a in section 3.3).

The velocity vector (so called "Newton") diagram, describing the kinematics of the reactive system, is depicted in Fig. 2a. We detected reactive signal at mass-to-charge (m/z) ratios m/z = 69 ($C_4H_5O^+$), 68 ($C_4H_4O^+$), 43 ($C_2H_3O^+$), 42 ($C_3H_6^+$, CH_2CO^+), 41 ($C_3H_5^+$), 30 (CH_2O^+), and 29 (HCO^+). The measured relative intensities at the CM angle ($\theta = 48°$) for these m/z values (at 17 eV) are 0.04, 0.21, 0.02, 0.14, 1.00, 0.12, and 0.13, respectively. The product LAB angular distributions, $N(\theta)$, were acquired only at m/z = 69, 68, 43, 42, 41 and 29; those at m/z = 68, 42, 41, and 29 are displayed in Fig. 2b, while the complete data set is reported in Fig. S1b† of the ESI. Exemplary TOF distributions at some selected LAB angles for m/z = 68, 42, 41, 30, and 29 are displayed in Fig. 2c (again, the complete TOF data set is reported in Fig. S2 and S3† of the ESI).

Most measurements were carried out by exploiting soft ionization at 17 eV electron energy, which was sufficient to suppress most of the interferences from the dissociative ionization processes of reactants and background gases; however, data at some masses were collected at both 70 eV and 17 eV for normalization purposes. The black continuous curves in Fig. 2b and c represent the global best-fit for the indicated m/z data, while the labeled color coded curves are the partial contributions from the various indicated products when using the best-fit CM product angular, $T(\theta)$, and translational energy, $P(E_T')$, distributions reported in Fig. 3 for the eight characterized product channels. We describe below, separately, how the information on the dynamics of the eight detected channels was derived.

3.2.1 The m/z = 69 and 68 data: H displacement and H_2 elimination channels. The occurrence of the H atom displacement channels, (3) and (4), and H_2 elimination channel, (5), was investigated at m/z = 69 ($C_4H_5O^+$) and 68 ($C_4H_4O^+$). Since the reactive signal at m/z = 69 was about five times lower than that at m/z = 68, the heavy co-products related to H displacement and H_2 elimination were explored at m/z = 68, for which the S/N was best. Notably, measurements at m/z = 68 permitted us to describe the dynamics of both channels, because they are characterized by very different kinematics, dynamics, and exothermicity. In fact, the co-product of H_2, namely C_4H_4O ($CH_2CHCHCO$, vinylketene), scatters over a more extended angular range compared to C_4H_5O, which is left by the light H atom, because of linear momentum conservation. Indeed, the Newton circles of C_4H_5O and C_4H_4O differ very significantly, with the former being much smaller (see Fig. 2a). While the angular distribution at m/z = 69 peaks at the CM angle and dies off on both sides to zero (see Fig. S1b†), reflecting only the C_4H_5O product(s) from channels (3) and (4), the angular distribution at m/z = 68, measured between 12° and 72° in the LAB frame (see Fig. 2b and S1b†), is also bell-shaped and peaks at $\theta_{CM} = 48°$ as the m/z = 69 distribution, indicating that at m/z = 68, the C_4H_5O

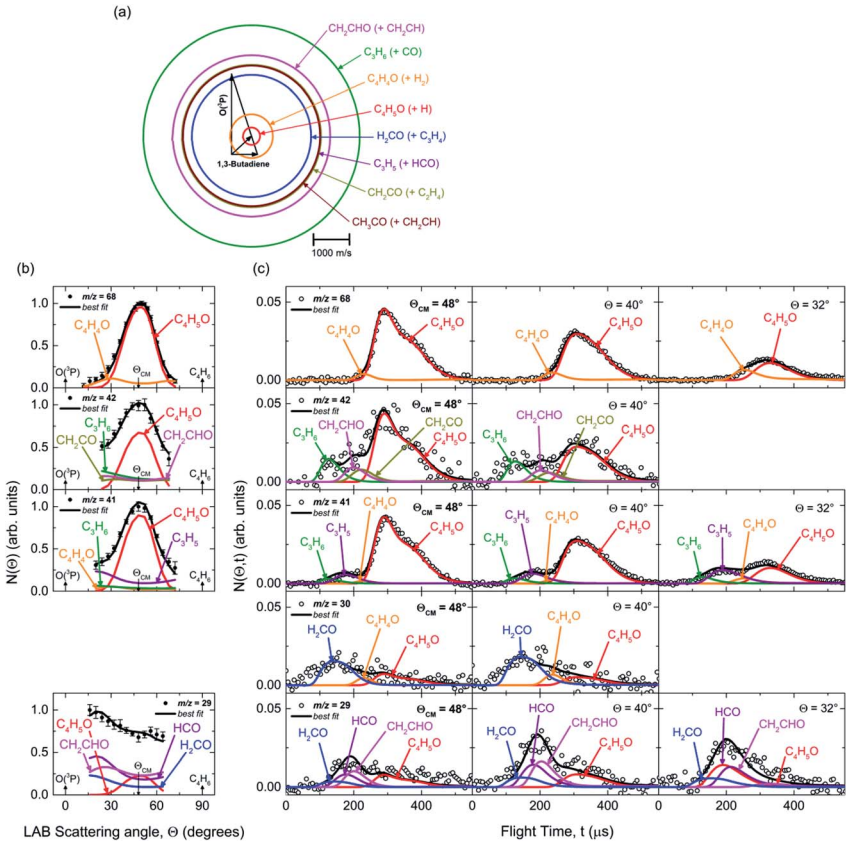

Fig. 2 (a) Velocity vector diagram for the $O(^3P)$ + 1,3-butadiene reaction (E_c = 32.6 kJ mol^{-1}). The color-coded circles, concentric to the CM, delimit the maximum velocity that the indicated primary products can attain in the CM frame by assuming that all the available energy (given by $E_c - \Delta H_0^0$) is channeled into product translational energy. Eight product channels were identified: C_4H_5O + H (red), C_4H_4O + H_2 (orange), C_3H_6 + CO (green), C_3H_5 + HCO (purple), CH_2CO + C_2H_4 (green-olive), CH_2CHO + C_2H_3 (pink), CH_3CO + CH_2CH (garnet), and H_2CO + C_3H_4 (blue). (b) LAB product angular distributions $N(\theta)$ measured at m/z = 68, 42, 41, and 29. Experimental error bars indicate $\pm 1\sigma$. (c) Product TOF distributions measured for m/z = 68 (70 eV), 42 (17 eV), 41 (17 eV), 30 (70 eV), and 29 (17 eV) at the indicated LAB angles θ. The partial contributions of different products at the five masses are indicated. Note that the integrated signal at $\theta_{CM} = 48°$ (at 17 eV) for m/z = 41 is seven times larger than that for m/z = 42, and five times larger than that for m/z = 68, as reflected in the S/N of the spectra. In (b) and (c), the black line superimposed on the experimental data corresponds to the global best-fit calculated using the CM functions shown in Fig. 3. The distinct contributions to the calculated global $N(\theta)$ (b) and $N(\theta,t)$ (c) are colored coded as in (a), and indicated with the formula of the corresponding product.

product is almost dominant; however, one can appreciate that the H channel contribution is not sufficient to reach the intensity measured on the wings, especially at angles smaller than θ_{CM}. This difference in intensity between the calculated C_4H_5O distribution and the experimental data suggests the presence of an additional primary product, besides the co-product of the H channel, and this can only correspond to the co-product of the H_2 channel, C_4H_4O, detected at its parent mass. This is corroborated by the TOF distributions measured at six

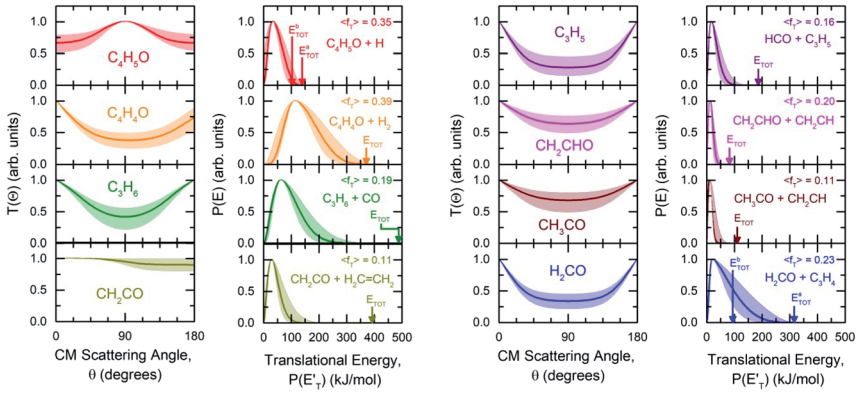

Fig. 3 First and third panel (from left): best-fit CM angular distributions of C_4H_5O, C_4H_4O, propene (C_3H_6), and ketene (CH_2CO), and of allyl (C_3H_5), vinoxy (CH_2CHO), acetyl (CH_3CO), and formaldehyde (H_2CO), respectively. Second and fourth panel: best-fit CM translational energy distributions for each corresponding channel. Color coding is as in Fig. 2. The arrows indicate the total energy (E_{TOT}) and $<f_T>$ the average translational energy fraction (referred to the most exothermic isomeric channel) determined for each reaction channel. The shaded areas represent the error bars determined for the best-fit CM functions.

different angles for the same m/z value (see Fig. S2†) with three of them shown in Fig. 2c. In these figures, the $m/z = 68$ TOF spectra exhibit a small, yet very significant fast shoulder whose relative intensity with respect to the slow, broad main peak increases as we move further away from the CM angle towards the wings of the angular distribution, which also confirms the formation of C_4H_4O from H_2 elimination.

The facts that the co-product of C_4H_4O has a mass twice that of the co-product of C_4H_5O, and that the H_2 channel (5) is much more exothermic and exhibits a much higher exit barrier than the H displacement channel(s) (3) and (4), are the characteristics which determine the broader angular distribution of C_4H_4O with respect to C_4H_5O in the LAB frame (see Fig. 2b) and its faster TOF distributions at the various LAB angles (see Fig. 2c). The large width of the C_4H_4O LAB angular distribution and the fast contribution to the TOF spectra determine the $P(E_T')$ peaking much further away from zero and extending to much higher energies than the $P(E_T')$ for the H forming channel, as can be clearly appreciated in Fig. 3. Notably, both channels exhibit a backward–forward symmetric $T(\theta)$ because both proceed *via* a long-lived complex mechanism,[75–77] but with different dynamics, which are reflected in the shapes of the corresponding $T(\theta)$: that of C_4H_5O is in fact sideways distributed (see below), while that of C_4H_4O is polarized (see Fig. 3). It should be noted that the experimental data do not permit the quantification of the relative contribution of the two C_4H_5O isomer products (channels (3) and (4)), but theory can disentangle them because they involve different pathways along the triplet PES (see the Discussion section). It should be noted that the heavy co-products of the H and H_2 channels are also observed at lower m/z ratios as daughter ions (see Fig. 2b and c, and the next section).

3.2.2 The $m/z = 43$, 42, and 41 data: C_3H_6 + CO, CH_2CO + C_2H_4, C_3H_5 + HCO, and CH_2CHO + C_2H_3 channels. At $m/z = 43$, 42, and 41, the angular distributions

peak around the CM angle (Fig. 2b and S1†), as with those at $m/z = 69$ and 68, but also exhibit wings in both the backward and forward directions, which indicate additional products from C–C bond breakage channels. These lighter products will scatter, by momentum conservation, over wider Newton circles than those of C_4H_5O and C_4H_4O (see Fig. 2a).

Concerning the $N(\theta)$ at $m/z = 43$ (see Fig. S1b†), the only possible product contributing to this mass, apart from the co-products of the H and H_2 channels, is $C_2H_3O^+$, which can be the only acetyl radical parent ion (CH_3CO^+), since it is known that vinoxy does not produce a stable parent ion (CH_2CHO^+) for electron energies >12 eV.[55] Notably, acetyl was also observed in the isomeric reaction $O(^3P)$ + 1,2-butadiene.[26] LAB angular distributions at $m/z = 42$ and 41 show a shape similar to that at $m/z = 43$ due to the large contribution of the H elimination channel (which is amplified in the LAB frame by a favorable CM → LAB Jacobian transformation[54,57]). However, in the $m/z = 42$ and 41 data, new reaction channels can also be identified, as demonstrated by the TOF distributions; in fact, these are very different from those recorded at $m/z = 68$, because, in addition to the slow peak due to the H and H_2 co-products, they also exhibit fast, broad components that reflect more than one C–C bond breaking channel. In fact, the fast peak at $m/z = 42$ (Fig. 2c and S2†) is unambiguously attributed, by energy and momentum conservation, to the propene product from channel (6), detected at its parent ion. Furthermore, the reactive signal between this fast peak and the C_4H_5O peak is attributed in a larger part to the vinoxy radical from channel (9), detected at its main (daughter) ion mass, and in a smaller part to ketene, detected at its parent ion mass, from channel (7). The occurrence of the propene channel (6) was also assessed through its (−1) daughter ion at $m/z = 41$ as a fast shoulder superimposed on a rather broad, slower peak centered at around 180 μs (see Fig. 2c). This peak cannot originate from the dissociative ionization of vinoxy and ketene, because the signal intensity at $m/z = 41$ is about seven times larger than that at $m/z = 42$, and ketene and vinoxy fragment little to the (−1) daughter ion at 17 eV (less than 30% at 70 eV). This important feature is rather attributed to the parent ion of the allyl radical (C_3H_5) from reaction channel (8) (C_3H_5 + HCO). Allyl is known to fragment little at 17 eV.[55,78]

3.2.3 The $m/z = 30$ and 29 data: H_2CO + C_3H_4 channels. For $m/z = 30$, because of the low signal intensity, only two TOF spectra at 70 eV were measured (see Fig. 2c). These spectra present a broad, fast peak which can be identified as being due to formaldehyde, dominantly from channel (12) (see below), and a slower, broad, less intense peak due to the daughter ions of the C_4H_4O and C_4H_5O products. The TOF data at $m/z = 29$ (Fig. 2c and S3†) show a slow small contribution of the C_4H_5O + H channel indicated by the small peak near the CM velocity (at ∼300 μs), a prominent peak at ∼200 μs, attributed to the HCO product (momentum matched with the $m/z = 41$ signal attributed to the allyl co-product C_3H_5) (channel (10)) and to the somewhat slower vinoxy from the CH_2CHO + vinyl channel (**9**), respectively, and a small fast shoulder corresponding to the daughter ion of H_2CO (channels (**11**) and (**12**)), which corroborates the $m/z = 30$ TOF.

3.2.4 Product angular and translational energy distributions in the CM frame. The derived best-fit product angular, $T(\theta)$, and translational energy, $P(E_T')$, distributions for the eight detected channels are depicted in Fig. 3. As can be seen, the majority of the $T(\theta)$s of the detected primary products are backward–forward symmetric in the 0–180° CM angular range, with varying degrees of polarization

(depending on the product), and this indicates that the corresponding reactive channels proceed *via* a long-lived complex mechanism, or rather, the corresponding intermediate lifetime is longer than 5–6 rotational periods of the decomposing complex.[75–77] Interestingly, the H elimination channel clearly presents a sideways distribution, indicating that this product is not formed on the same plane as the reactants (*i.e.*, the reaction is not co-planar), but rather the atomic hydrogen is emitted perpendicularly to the plane of the heavy atoms,[75–77] and this is corroborated by the theoretical calculations of the TS geometries (see Fig. S5† in the ESI and the Discussion). In Fig. 3, the average translational energy fractions $\langle f_T \rangle$ and the total available energy (E_{TOT}), given by $E_c - \Delta H_0^0$, are also indicated for each channel. The high $\langle f_T \rangle$ of 0.35 and 0.39 for the reaction channels (**3**, **4**) and (5) (C_4H_5O + H and C_4H_4O + H_2) reflect the presence of high exit energy barriers in the relevant triplet/singlet PESs (see Fig. 1) and are corroborated by theory (see the Discussion). The size of $\langle f_T \rangle$ (<0.2) for the other channels indicates that the molecular/radical products are internally highly excited.

3.2.5 Product branching fractions. The most useful information obtainable from CMB experiments on the dynamics of a multichannel reaction are the branching fractions of the various channels. The BFs have been estimated following the procedure developed by Schmoltner *et al.*[79] and applied by us successfully to numerous reactions of $O(^3P)$ with unsaturated hydrocarbons.[16–28,80] The derived BFs for the $O(^3P)$ + 1,3-butadiene reaction at $E_c = 32.6$ kJ mol^{-1} are reported in Table 1.

As can be seen, the $O(^3P)$ + 1,3-butadiene reaction mainly leads to the formation of HCO + C_3H_5 (formyl + allyl, BF = 36.2 ± 12.0%) and CO + C_3H_6 (CO + propene, BF = 20.2 ± 7.0%). Other important products formed are formaldehyde + $^3CH_2CHCH$ (H_2CO + C_3H_4, BF = 18.6 ± 9.3%), vinoxy + vinyl radicals (CH_2CHO + C_2H_3, BF = 9.5 ± 3.3%), ketene + ethylene (CH_2CO + C_2H_4, BF = 6.9 ± 3.4%), and the atomic hydrogen displacement channel (C_4H_5O + H, BF = 6.2 ± 2.2%). Minor channels are the formation of molecular hydrogen (C_4H_4O + H_2, BF = 1.8 ± 0.6%), as well as the formation of acetyl + vinyl radicals (CH_3CO +

Table 1 Product branching fractions (BFs) of the $O(^3P)$ + 1,3-butadiene reaction at E_c = 32.6 kJ mol^{-1}, compared to statistical RRKM/ME results in CMB conditions and in thermal conditions at 300 K and 1000 K at 1 bar. (T) and (S) refer to triplet and singlet PESs, respectively

Product channel	CMB expt. E_c = 32.6 kJ mol^{-1} BF (%)	RRKM/ME E_c = 32.6 kJ mol^{-1} BF (%)	RRKM/ME 300 K, 1 bar BF (%)	RRKM/ME 1000 K, 1 bar BF (%)
$CH_2CHCHCHO$ + H	6.2 ± 2.2	13.7 (T)	5.5 (T)	18.0 (T)
$CH_2CHCOCH_2$ + H		2.2 (T)	2.3 (T)	8.6 (T)
C_4H_4O + H_2	1.8 ± 0.6	—	—	—
C_3H_6 + CO	20.2 ± 7.0	22.8 (S)	19.4 (S)	6.7 (S)
CH_2CO + C_2H_4	6.9 ± 3.4	—	—	—
C_3H_5 + HCO	36.2 ± 12.0	44.4 (S)	20.3 (S)	19.0 (S)
CH_2CHO + C_2H_3	9.5 ± 3.3	6.3 (T)	6.3 (T)	27.4 (T)
CH_3CO + C_2H_3	0.4 ± 0.2	0.5 (S)	—	0.4 (S)
H_2CO + C_3H_4	18.6 ± 9.3	9.2 (T)	1.9 (T)	20.1 (T)

C_2H_3, BF = 0.4 ± 0.2%). In Table 1, the experimental BFs are compared with the theoretical BFs calculated for the conditions of the CMB experiment: they will be discussed in the next section.

3.3 Master equation simulations and discussion

The BFs determined through ME simulations in CMB conditions are compared with experimental results in Table 1. On the whole, it can be noted that the agreement is quite good, with most of the calculated BFs falling within the uncertainty bounds of the experimental determinations. It is useful here to compare and discuss experimental measurements and theoretical predictions channel by channel and with respect to our previous investigations of the $O(^3P)$ + alkene reactions.[20,25] The main reaction channels in CMB conditions are active on the singlet PES and lead to the formation of HCO + C_3H_5 and C_3H_6 + CO in a nearly 2 to 1 ratio (experimentally 1.8 : 1.0, theoretically 1.9 : 1.0). These two reaction channels account for about 60% of the reactive flux and are both accessed after ISC from the 3-butenal well. It is important to note that a significant portion of this reaction flux comes from isomerization from ^{3}W2 to ^{3}W1 through ^{3}W3 and successive ISC to the singlet PES. About 60% of the flux accessing the triplet PES from addition to the central carbon atom follows this reaction pathway. The agreement between experiments and theory is quite good. For the CO + C_3H_6 channel, the $P(E_T')$ exhibits a late onset and peaks at 63 kJ mol^{-1}, which indicates the presence of a significant exit barrier. This is corroborated by theory, which indeed finds a very significant exit energy barrier (^{1}TS3) of ~200 kJ mol^{-1} with respect to the products (Fig. 1b). The symmetric $T(\theta)$ is indicative of a long-lived complex mechanism, consistent with the large stability of ^{1}W2. In contrast, the dominant radical channel C_3H_5 + HCO, which has a similarly polarized, symmetric $T(\theta)$, exhibits a $P(E_T')$ which rises very quickly and peaks at a very low energy (~17 kJ mol^{-1}) and dies off at less than one half of the total available energy, with only 16% of the available energy released in product translation, a feature expected for the barrierless decomposition of the intermediate ^{1}W2.

The reactions leading to H loss take place on the triplet PES and are expected, according to theoretical calculations, to account for about 16% of the reactive flux. This is higher than the BF found experimentally for this channel (6.2 ± 2.2%). This difference in BFs for the H channels was also found in our investigations of the $O(^3P)$ + 1-butene and $O(^3P)$ + propene reactions.[20,25] In both these studies, it was attributed to a non-RRKM behavior of this reaction channel, determined probably by a slow rate of thermalization of the C–H stretching modes of the methylene group following terminal O addition. Apart from the difference in the BFs, there is good agreement between the calculated structures and energy barriers of the TSs and experimental evidence. The best-fit $T(\theta)$ for the C_4H_5O product exhibits a pronounced sideways peaking, which indicates that the H atom is emitted orthogonally to the plane of the molecular intermediate at ^{3}TS2 (also at ^{3}TS10), and the best-fit $P(E_T')$ peaks away from zero, at about 34 kJ mol^{-1}, which is consistent with the high exit barriers from both ^{3}W1 and ^{3}W2, and extends up to about 135 ± 10 kJ mol^{-1}. This is well matched by the total available energy for channel (3) (135.1 kJ mol^{-1}), given by the sum of the reaction ΔH_0^0 (102.5 kJ mol^{-1}) and the collision energy (32.6 kJ mol^{-1}). The high average

fraction of total available energy released in translation (<f_T>= 0.34, referring to channel (3)) reflects, in fact, a high exit potential barrier that the theory finds of 32.5 kJ mol^{-1} for channel (3) and 43.1 kJ mol^{-1} for channel (4), with respect to products (Fig. 1a). The sideways dynamics for H emission from transition state ^{3}TS2 (and also ^{3}TS10) are corroborated by the calculated structure of ^{3}TS2 and ^{3}TS10, which show that the direction of the departing H atom is about orthogonal to the molecular plane (see Fig. S5† in the ESI).

The fourth channel in the order of relevance predicted by the ME simulations is that leading to formaldehyde + vinylmethylene (channel (12)). The agreement between simulations and experimental BFs is reasonable, with the theoretical results (9.2%) underestimating the experimental determination (18.6 ± 9.3%), but within the lower limit of its uncertainty. This difference is similar to what was found in our study of O(^{3}P) + propene,[20] while experiments and theory were in good agreement for the O(^{3}P) + 1-butene system.[25] We note that the derived $P(E_T')$ peaks at about 20 kJ mol^{-1} (Fig. 3), which reflects a relatively small exit barrier, consistent with the formation of H_2CO + $^3CH_2CHCH$ on the triplet PES from ^{3}W1 (Fig. 1a). However, the $P(E_T')$ extends up to about 250 ± 70 kJ mol^{-1}, which is beyond the total available energy of channel (12), whose E_{TOT} is ~95 kJ mol^{-1}. The experiments appear then to suggest that not all of the H_2CO channel originates from the triplet PES, but a fraction of it could originate from a more exoergic pathway, as that on the singlet PES, after ISC, leading to H_2CO + CH_2CCH_2 (allene) (channel (11)) (see Fig. 1b). Notably, comparable fractions of H_2CO produced on the triplet PES were also observed in the reactions of O(^{3}P) with ethylene,[19] allene,[23] propene,[20] 1-butene,[25] and 1,2-butadiene.[26]

The main channel on the triplet PES arising from addition to the terminal carbon atom is that leading to vinoxy + vinyl, for which both experiments and theory are in good agreement (see Table 1). The corresponding $P(E_T')$ peaks at ~13 kJ mol^{-1}, which is consistent with the calculated exit barrier, and reflects an average fraction of energy in product translation of ~20%. With the $T(\theta)$ being symmetric, this channel also proceeds *via* a long-lived complex mechanism.

The most significant difference between experiment and theory concerns the CH_2CO + C_2H_4 molecular channel, for which the experimental BFs (6.9 ± 3.4%) are much larger than those computed theoretically for this reaction. This suggests that it is possible that a reaction path that we could not find despite an extensive PES investigation is missing from those reported in Fig. 1.

Experimental evidence was also found for two other minor channels, leading to H_2 + C_4H_4O (vinylketene) and CH_3CO + C_2H_3 formation. While the latter's experimental BFs are well predicted by theory, this is not the case for the H_2 channel (see Table 1). This may be due to the simplified form of the PES used in the ME simulations, in which we did not investigate in detail the reaction dynamics that follow ISC. In our previous study of O(^{3}P) + propene,[20] we had in fact found that some molecular hydrogen can be produced through elimination from the diradical complex formed upon ISC.

Finally, the extent of ISC in O(^{3}P) + 1,3-butadiene, estimated experimentally and theoretically in CMB conditions, amounts to about 66 ± 20% and 67%, respectively. This is not surprising considering that the extent of ISC in other O(^{3}P) reactions, at comparable E_cs with unsaturated 4C hydrocarbons, such as 1-butene[25] and 1,2-butadiene,[26] is about 50% and 70%, respectively. Notably, ISC is about 50% in O + ethylene[19] and about 90% in O + allene.[23]

The product distribution is different from what was observed in any of the four-carbon atom systems so far investigated, namely O + 1-butene[25] and O + 1,2-butadiene,[26] at comparable E_cs. In O + 1-butene, the CO channel was not observed, while HCO formation, although not the minor channel, was detected in a smaller amount (BF = 17%). On the other hand, in O + 1,2-butadiene,[26] the CO channel was detected as the main channel (BF = 49%) while HCO formation was the minor channel and was almost negligible (BF = 1%). Even if the three hydrocarbons (1-butene, 1,2-butadiene, and 1,3-butadiene) present different structures, some similarities would be expected in their product BFs. However, the results for 1,3-butadiene seem closer to those observed for the reaction of 1-butene[25] than 1,2-butadiene.[26] This is reasonable, since with two non-consecutive double bonds, the reactivity of 1,3-butadiene will be more similar to that of a molecule with only one terminal unsaturated bond.

Master equation simulations were finally performed in thermal equilibrium conditions in order to determine the temperature and pressure dependent rate constants to be used for the kinetic modeling of this system. Simulations were performed in the 300–2200 K temperature range at 0.1, 1, and 10 bar. The calculated total rate constants are reported in Fig. 4a, together with the contributions for terminal and central addition and for H abstraction. The rate constants calculated as a function of temperature at 1 bar for the most relevant channels are reported in Fig. 4b, while those calculated at 0.1 and 10 bar are reported in the ESI.† It is found that the extent of ISC decreases with the increase of the temperature from 84% at room temperature to 26% at 1000 K and 1 bar. At 1000 K, the main termination channels lead to $H_2CO + CH_2CHCH$ and $CO + C_3H_6$ formation and account for about 27% of the reactive flux, while the $H + C_4H_5O$ and $HCO + C_3H_5$ channels contribute about 20% each and the main reaction channel becomes $C_2H_3 + CH_2CHO$. Collisional stabilization is important only at low temperatures and accounts for 44% of the reaction flux at 300 K and 1 bar, which decreases to 10% already at 500 K (see ESI†). At 10 bar and 500 K, collisional stabilization is still important, accounting for about 57% of the total reaction flux, which decreases to 24% at 750 K (see ESI†). It can thus be inferred

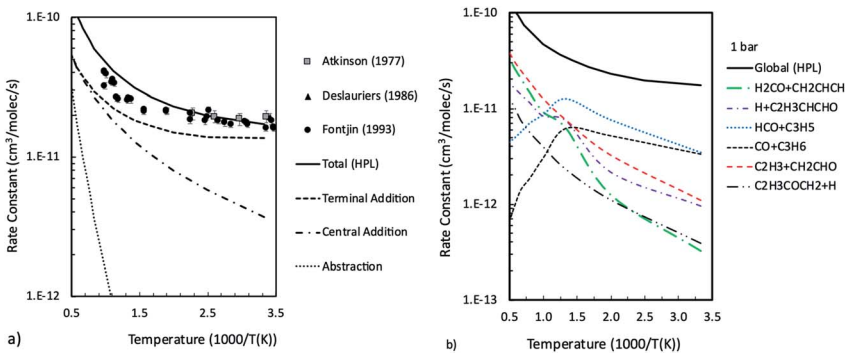

Fig. 4 Total rate constants for the $O(^3P)$ + 1,3-butadiene reaction compared with experimental data[48,50,51] and contributions of addition to central and terminal carbon atoms and abstraction (a), and channel specific rate constants computed as a function of temperature at 1 bar (b).

that collisional stabilization can become relevant in combustion conditions at relatively low temperatures and only at pressures higher than 10 bar. The reason is that, since collisional stabilization is a termination reaction alternative to the HCO + C_3H_5 branching channel, it is possible that it may influence the system reactivity, such as, for example, high pressures delay ignition times, to some extent.

4. Conclusion

The dynamics of the O(^{3}P) + 1,3-butadiene reaction were investigated through a synergic experimental and theoretical approach, finding a good agreement between CMB results and statistical calculations of the product BFs. It was found that the reaction kinetics for this system are rich, with many active channels with relevant BFs both on the singlet and the triplet PESs. The main reaction channels lead to the formation of HCO + C_3H_5 and CO + C_3H_6, which account for about 60% of the total reactive flux both experimentally and theoretically, followed by H + C_4H_5O, H_2CO + CH_2CHCH, and C_2H_3 + CH_2CHO. The ME simulations show that, differently from what was found for the O(^{3}P) + alkene reaction class, isomerization reactions are active on the triplet PES when it is accessed through addition to the central carbon atom. The reason why this happens is that, because of the presence of two conjugated unsaturated bonds, it is possible for the adduct formed by oxygen and 1,3 butadiene upon addition to isomerize to form an oxirane triplet well, whose formation requires only a bond forming reaction, thus without any H transfer step involved. It seems thus that the reaction mechanism we proposed to interpret the reactivity of alkenes with atomic oxygen,[31] according to which the reactivity on triplet PESs is governed by bond breaking reactions and ISC, should be extended to conjugated dienes to account for the scrambling of atomic oxygen between the possible addition sites. This mechanism thus favors the formation of the lowest energy triplet isomer. However, as simulations performed in thermal equilibrium show, when the temperature increases, the relevance of decomposition to C_2H_3 + CH_2CHO increases correspondingly, as it becomes the dominant channel for oxygen addition to the central carbon atom. With respect to existing kinetic models of the O(^{3}P) + 1,3-butadiene reaction, we find that in thermal conditions, in addition to the channels already included in existing models, the formation of HCO + C_3H_5 can also play a relevant role. The thermal simulations show that the system behavior as a function of temperature is characterized by low and high temperature regimes, with the first being dominated by ISC to the singlet PES and the second by the reactivity on the triplet PES. Interestingly, the transition between the two regimes takes place at about 1000 K, thus at a temperature that is of key relevance for combustion modeling. As rate constants in this transition regime assume a significant non-Arrhenius behavior, it will be interesting to test if and how this affects the oxidation kinetics of this system once the calculated channel-specific rate constants are introduced in kinetic models.

Conflicts of interest

There are no conflicts to declare.

Acknowledgements

Financial support from Italian "Ministry of University and Research" (MUR) (PRIN 2017, MAGIC DUST, Prot. 2017PJ5XXX) is gratefully acknowledged. P. R., A. C., N. B., and P. C. acknowledge support also from the Italian MUR and the University of Perugia within the program “Department of Excellence-2018-2022-Project AMIS”.

References

1 H. Schobert, *Chemistry of Fossil Fuels and Biofuels*, Cambridge University Press, Cambridge, UK., 2013.
2 M. Frenklach, D. W. Clary, W. C. Gardiner and S. E. Stein, *Symp. (Int.) Combust., [Proc.]*, 1988, **21**, 1067–1076.
3 W. C. Gardiner, *Gas-Phase Combustion Chemistry*, Springer, New York, 2000.
4 K. Kohse-Höinghaus, P. Oßwald, T. A. Cool, T. Kasper, N. Hansen, F. Qi, C. K. Westbrook and P. R. Westmoreland, *Angew. Chem., Int. Ed.*, 2010, **49**, 3572–3597.
5 J. M. Simmie, *Prog. Energy Combust. Sci.*, 2003, **29**, 599–634.
6 P. Zhao, W. Yuan, H. Sun, Y. Li, A. P. Kelley, X. Zheng and C. K. Law, *Proc. Combust. Inst.*, 2015, **35**, 309–316.
7 C. W. Zhou, Y. Li, U. Burke, C. Banyon, K. P. Somers, S. Ding, S. Khan, J. W. Hargis, T. Sikes, O. Methieu, E. L. Petersen, M. AlAbbad, A. Farooq, Y. Pan, Y. Zhang, Z. Huang, J. Lopez, Z. Loparo, S. S. Vasu and H. J. Curran, *Combust. Flame*, 2018, **197**, 423–438.
8 W. K. Metcalfe, S. Dooley and F. L. Dryer, *Energy Fuels*, 2011, **25**, 4915–4936.
9 J. Yiguang and S. Wenting, *Prog. Energy Combust. Sci.*, 2015, **48**, 21–83.
10 R. P. Wayne, *Chemistry of Atmospheres: an Introduction to the Chemistry of the Atmospheres of Earth, the Planets, and their Satellites*, Oxford University Press, Oxford, UK., 3rd edn, 2000.
11 A. M. Shaw, *Astrochemistry: from Astronomy to Astrobiology*, Wiley, 2007.
12 A. G. G. M. Tielens, *Rev. Mod. Phys.*, 2013, **85**, 1021–1081.
13 A. Occhiogrosso, S. Viti and N. Balucani, *Mon. Not. R. Astron. Soc.*, 2013, **432**, 3423–3430.
14 M. Dobrijevic, E. Hebrard, J. C. Loison and K. M. Hickson, *Icarus*, 2014, **228**, 324–346.
15 L. M. Lara, E. Lellouch, M. Gonzales, R. Moreno and M. A. Rengel, *Astron. Astrophys.*, 2014, **566**, A143.
16 P. Casavecchia, G. Capozza, E. Segoloni, F. Leonori, N. Balucani and G. G. Volpi, *J. Phys. Chem. A*, 2005, **109**, 3527–3530.
17 B. Fu, Y.-C. Han, J. M. Bowman, L. Angelucci, N. Balucani, F. Leonori and P. Casavecchia, *Proc. Natl. Acad. Sci. U. S. A.*, 2012, **109**, 9733–9738.
18 B. Fu, Y.-C. Han, J. M. Bowman, F. Leonori, N. Balucani, L. Angelucci, A. Occhiogrosso, R. Petrucci and P. Casavecchia, *J. Chem. Phys.*, 2012, **137**, 22A532.
19 N. Balucani, F. Leonori, P. Casavecchia, B. Fu and J. M. Bowman, *J. Phys. Chem. A*, 2015, **119**, 12498–12511.
20 F. Leonori, N. Balucani, V. Nevrly, A. Bergeat, S. Falcinelli, G. Vanuzzo, P. Casavecchia and C. Cavalloti, *J. Phys. Chem. C*, 2015, **119**, 14632–14653.

21 G. Vanuzzo, N. Balucani, F. Leonori, D. Stranges, V. Nevrly, S. Falcinelli, A. Bergeat, P. Casavecchia and C. Cavallotti, *J. Phys. Chem. A*, 2016, **120**, 4603–4618.
22 I. Gimondi, C. Cavallotti, G. Vanuzzo, N. Balucani and P. Casavecchia, *J. Phys. Chem. A*, 2016, **120**, 4619–4633.
23 F. Leonori, A. Occhiogrosso, N. Balucani, A. Bucci, R. Petrucci and P. Casavecchia, *J. Phys. Chem. Lett.*, 2012, **3**, 75–80.
24 G. Vanuzzo, N. Balucani, F. Leonori, D. Stranges, S. Falcinelli, A. Bergeat, P. Casavecchia, I. Gimondi and C. Cavallotti, *J. Phys. Chem. Lett.*, 2016, **7**, 1010–1015.
25 A. Caracciolo, G. Vanuzzo, N. Balucani, D. Stranges, P. Casavecchia, L. Pratali Maffei and C. Cavallotti, *J. Phys. Chem. A*, 2019, **123**, 9934–9956.
26 A. Caracciolo, G. Vanuzzo, N. Balucani, D. Stranges, S. Tanteri, C. Cavallotti and P. Casavecchia, *Chin. J. Chem. Phys.*, 2019, **32**, 113–122.
27 C. Cavallotti, C. De Falco, L. P. Maffei, A. Caracciolo, G. Vanuzzo, N. Balucani and P. Casavecchia, *J. Phys. Chem. Lett.*, 2020, **11**, 9621–9628.
28 G. Vanuzzo, A. Caracciolo, T. K. Minton, N. Balucani, P. Casavecchia, C. de Falco, A. Baggioli and C. Cavallotti, *J. Phys. Chem. A*, 2021, **125**, 8434–8453.
29 J. D. Savee, O. Welz, C. A. Taatjes and D. L. Osborn, *Phys. Chem. Chem. Phys.*, 2012, **14**, 10410–10423.
30 C. A. Taatjes, D. L. Osborn, T. Selby, G. Meloni, A. J. Trevitt, E. Epifanovsky, A. I. Krylov, B. Sirjean, E. Danes and H. Wang, *J. Phys. Chem. A*, 2010, **114**, 3355–3370.
31 L. Pratali Maffei, C. Cavallotti, A. Caracciolo, N. Balucani and P. Casavecchia, *Fuel*, 2020, **263**, 116536.
32 K. Ramasesha, J. D. Savee, J. Zádor and D. L. Osborn, *J. Phys. Chem. A*, 2021, **125**, 9785–9801.
33 C. Cavallotti, F. Leonori, N. Balucani, V. Nevrly, A. Bergeat, S. Falcinelli, G. Vanuzzo and P. Casavecchia, *J. Phys. Chem. Lett.*, 2014, **5**, 4213–4218.
34 Y. Zhang, J. Cai, L. Zhao, J. Yang, H. Jin, Z. Cheng, Y. Li, L. Zhang and F. Qi, *Combust. Flame*, 2012, **159**, 905–917.
35 Y. Fenard, G. Dayma, F. Halter, F. Foucher, Z. Serinyel and P. Dagaut, *Energy Fuels*, 2015, **29**, 1107–1118.
36 M. Schenk, L. Leon, K. Moshammer, P. Osswald, T. Zeuch, L. Seidel, F. Mauss and K. Kohse-Hoinghaus, *Combust. Flame*, 2013, **160**, 487–503.
37 L. Ruwe, K. Moshammer, N. Hansen and K. Kohse-Hoinghaus, *Combust. Flame*, 2017, **175**, 34–46.
38 C.-W. Zhou, Y. Li, E. O'Connor, K. P. Somers, S. Thion, C. Keesee, O. Mathieu, E. I. Petersen, T. A. DeVerter, M. A. Oehlschlaeger, G. Kukkadapu, C.-J. Sung, M. Alrefae, K. Khaled, A. Farooq, P. Dirrenberger, P.-A. Glaude, F. Battin-Leclerc, J. Santner, Y. Ju, T. Held, F. M. Haas, F. L. Dryer and H. J. Curran, *Combust. Flame*, 2016, **167**, 353–379.
39 Z. J. Buras, E. E. Dames, S. S. Merchant, G. Liu, R. M. Elsamra and W. H. Green, *J. Phys. Chem. A*, 2015, **119**, 7325–7338.
40 Y. Li, C.-W. Zhou, K. P. Somer, K. Zhang and H. J. Curran, *Proc. Combust. Inst.*, 2017, **36**, 403–411.
41 Y. Li, C.-W. Zhou and H. J. Curran, *Combust. Flame*, 2017, **181**, 198–213.
42 C. Huang, B. Yang and F. Zhang, *Combust. Flame*, 2017, **184**, 167–175.
43 R. L. Melnick and J. Huff, *Rev. Environ. Contam. Toxicol.*, 1992, **124**, 111–144.

44 US Environmental Protection Agency (EPA), *Health Effects Notebook for Hazardous Air Pollutants: 1,3-butadiene*, retrieved April 2020, **https://www.epa.gov/haps/health-effects-notebook-hazardous-air-pollutants**.
45 I. Kirshenbaum, *Encyclopedia of Chemical Technology*, John Wiley & Sons, New York, 3nd edn, 1978, vol. 4.
46 J. J. Havel and K. H. Chan, *J. Org. Chem.*, 1974, **39**, 2439–2441.
47 X. S. Nip, D. L. Singleton and R. J. Cvetanovic, *Can. J. Chem.*, 1979, **57**, 949–952.
48 R. Atkinson and J. N. Pitts Jr, *J. Chem. Phys.*, 1977, **67**, 2492–2495.
49 K. Sugawara, Y. Ishikawa and S. Sato, *Bull. Chem. Soc. Jpn.*, 1980, **53**, 1344–1351.
50 H. Deslauriers and G. J. Collin, *Can. J. Chem.*, 1986, **64**, 1925–1929.
51 G. Y. Adusei and A. Fontijn, *J. Phys. Chem.*, 1993, **97**, 1406–1408.
52 A. Laskin, H. Wang and C. K. Law, *Int. J. Chem. Kinet.*, 2000, **32**, 589–614.
53 M. Alagia, N. Balucani, P. Casavecchia, D. Stranges and G. G. Volpi, *J. Chem. Soc., Faraday Trans.*, 1995, **91**, 575–596.
54 P. Casavecchia, *Rep. Prog. Phys.*, 2000, **63**, 355–414.
55 P. Casavecchia, F. Leonori, N. Balucani, R. Petrucci, G. Capozza and E. Segoloni, *Phys. Chem. Chem. Phys.*, 2009, **11**, 46–65.
56 N. Balucani, G. Capozza, F. Leonori, E. Segoloni and P. Casavecchia, *Int. Rev. Phys. Chem.*, 2006, **25**, 109–163.
57 P. Casavecchia, F. Leonori and N. Balucani, *Int. Rev. Phys. Chem.*, 2015, **34**, 161–204.
58 S. J. Sibener, R. J. Buss, C. Y. Ng and Y. T. Lee, *Rev. Sci. Instrum.*, 1980, **51**, 167–182.
59 M. Alagia, V. Aquilanti, D. Ascenzi, N. Balucani, D. Cappelletti, L. Cartechini, P. Casavecchia, F. Pirani, G. Sanchini and G. G. Volpi, *Isr. J. Chem.*, 1997, **37**, 329–342.
60 S. J. Klippenstein and C. Cavallotti, *Comput.-Aided Chem. Eng.*, 2019, **45**, 115–167.
61 J.-D. Chai and M. Head-Gordon, *Phys. Chem. Chem. Phys.*, 2008, **10**, 6615–6620.
62 J. M. L. Martin, *Chem. Phys. Lett.*, 1996, **259**, 669–678.
63 C. Cavallotti, M. Pelucchi, Y. Georgievskii and S. J. Klippenstein, *J. Chem. Theory Comput.*, 2019, **15**, 1122–1145.
64 M. Frisch, *et al.*, *Gaussian 16, Revision C.01*, 2016.
65 H.-J. Werner, *et al.*, *MOLPRO, version 2020.2, a package of ab initio programs*, see https://www.molpro.net, 2010.
66 Y. Georgievskii and S. J. Klippenstein, *J. Phys. Chem. A*, 2003, **107**, 9776–9781.
67 J. N. Harvey, *Phys. Chem. Chem. Phys.*, 2007, **9**, 331–343.
68 C. Zener, *Proc. R. Soc. London, Ser. A*, 1932, **137**, 696–702.
69 A. Barbato, C. Seghi and C. Cavallotti, *J. Chem. Phys.*, 2009, **130**, 074108.
70 D. Polino and C. Cavallotti, *J. Phys. Chem. A*, 2011, **115**, 10281–10289.
71 A. W. Jasper, *Int. J. Chem. Kinet.*, 2020, **52**, 387–402.
72 H. Sabbah, L. Biennier, I. R. Sims, Y. Georgievskii, S. J. Klippenstein and I. W. M. Smith, *Science*, 2007, **317**, 102–105.
73 X. Li, A. W. Jasper, J. Zádor, J. A. Miller and S. J. Klippenstein, *Proc. Combust. Inst.*, 2017, **36**, 219–227.
74 J. Shu, D. S. Peterka, S. R. Leone and M. Ahmed, *J. Phys. Chem. A*, 2004, **108**, 7895–7902.
75 R. D. Levine, *Molecular Reaction Dynamics*, Cambridge University Press, 2005.

76 W. B. Miller, S. A. Safron and D. R. Herschbach, *Discuss. Faraday Soc.*, 1967, **44**, 108–123.
77 G. A. Fisk, J. D. McDonald and D. R. Herschbach, General discussion, *Discuss. Faraday Soc.*, 1967, **44**, 228–230.
78 F. Leonori, N. Balucani, G. Capozza, E. Segoloni, D. Stranges and P. Casavecchia, *Phys. Chem. Chem. Phys.*, 2007, **9**, 1307–1311.
79 A. M. Schmoltner, P. M. Chu and Y. T. Lee, *J. Chem. Phys.*, 1989, **91**, 5365–5373.
80 H. Pan, K. Liu, A. Caracciolo and P. Casavecchia, *Chem. Soc. Rev.*, 2017, **46**, 7517–7547.